TEST SAMPLE ACCURACY SCALES WITH TRAINING SAMPLE DENSITY IN NEURAL NETWORKS

Xu Ji Mila
Razvan Pascanu DeepMind
Devon Hjelm Mila, MSR
Balaji Lakshminarayanan Google Brain
Andrea Vedaldi Oxford University

ABSTRACT

Intuitively, one would expect accuracy of a trained neural network's prediction on test samples to correlate with how densely the samples are surrounded by seen training samples in representation space. We find that a bound on empirical training error smoothed across linear activation regions scales inversely with training sample density in representation space. Empirically, we verify this bound is a strong predictor of the inaccuracy of the network's prediction on test samples. For unseen test sets, including those with out-of-distribution samples, ranking test samples by their local region's error bound and discarding samples with the highest bounds raises prediction accuracy by up to 20% in absolute terms for image classification datasets, on average over thresholds.

1 INTRODUCTION

When do trained models make mistakes? Intuitively, one expects higher prediction error for test samples that are more *novel*, compared to seen training data. For neural network inference models, one measure of sample novelty is distance from training samples in representation space, according to some distance metric k. Integrated over all training samples, this corresponds to the sample falling in a low density region in the metric space defined by k. A number of existing works on detecting out-of-distribution samples relate to this idea. For instance Lee et al. (2018) and Tack et al. (2020) use distance to estimated modes in network representation space as a measure of prediction unreliability. In non-parametric Gaussian Process inference (Rasmussen, 2003), prediction certainty corresponds exactly to local density of training samples. The idea of this work is to derive and empirically test a similar measure of prediction unreliability for ReLU neural networks.

Since the input space of a ReLU network can be partitioned into linear activation regions (Montúfar et al., 2014) such that each region is mapped to a distinct linear function that uses a different parameterization or subset of network weights - which for convenience we call the subfunctions of the network - one could cast the novelty or unreliability of a sample as a bound on error of the specific subfunction it induces. Unlike in error bounding for model selection, the objective is to take a pre-trained model and rank test samples, so the model is fixed. For deep networks, test samples typically fall in linear activation regions unpopulated by empirical training samples, so bounds that are a function of empirical training error are undefined. We propose to smooth the empirical error by taking a weighted average of empirical errors across activation regions where the weighting is defined by a function k of representation distance. Constructing a bound on smooth empirical error yields a quantity that scales exactly with the inverse of density of training samples in the representation space defined by k.

There are many possible ways to partition a neural network. An argument against making the partitioning more coarse than linear activation regions is reduction in discriminativity; in the extreme case, casting the network as a single subfunction results in the same error bound for all samples. An argument against making the partitioning more finegrained is linear functions are already the least complex class of parametric functions; there is no way to further subdivide a linear activation region such that the functions computed are different, as each input in the region implicates exactly the same parameters. However, an interesting direction for future work is extending the idea of density-as-reliability to density in continuous space, rather than of discrete partitions, which would require a different bound to the one used in this work.

Figure 1 illustrates our approach for a model trained on the half moons dataset. Considering the model as a composition of individual functions allows the discrimination of risk based on input region.

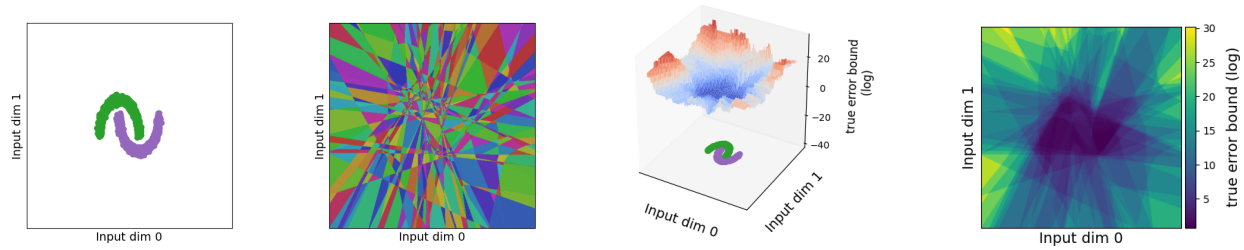

(a) (b) (c) (d)

Figure 1: Shattering a neural network trained on the halfmoons dataset into co-dependent linear subfunctions to obtain a heatmap of unreliability across the input space. The model is a MLP with two hidden ReLU layers of 32 units each. (a) Training data. (b) Linear activation regions. (c) Subfunction smooth error bound as unreliability. (d) Unreliability heatmap in 2D.

2 Input-dependent unreliability

2.1 Notation

Let $f : \mathcal{X} \to \mathcal{Y}$ be a piecewise linear neural network comprised of linear functions and ReLU activation functions. Let $V = (v_j)_{1 \leq j \leq M}$, ordered according to any fixed ordering, be the set of M ReLUs in f where $\forall j : v_j : \mathcal{X} \to \{0, 1\}$ is 1 if the ReLU is positive valued when $f(x)$ is computed, and 0 otherwise. Let patterns set $P \subset \{0, 1\}^M$, $P = (p_i)_{1 \leq i \leq C}$ be the set of all feasible ReLU activation decisions, meaning all possible binary patterns induced by traversing the input space $\mathcal{X}$. In general this is not equal to the full bit space $\{0, 1\}^M$, and tractably computing it exactly is an open problem (Montúfar et al., 2014). There is a bijection between these patterns and the linear activation regions of the network, as each linear activation region is uniquely determined by the set of ReLU activation decisions (Raghu et al., 2017). Let activation region a_i correspond to pattern p_i:

$$a_i \triangleq \{x \in \mathcal{X} \quad | \quad \forall j \in [1, M] : p_i^j = v_j(x)\}, \tag{1}$$

Each pattern p_i defines a distinct linear function $h_i : \mathcal{X} \to \mathcal{Y}$, or *subfunction*, by the replacement of the ReLU corresponding to each v_j (non-linear) by the identity function if $p_i^j = 1$ or the zero function otherwise (linear). Let the set of all subfunctions be $H = (h_i)_{1 \leq i \leq C}$, ordered identically to P. Since activation regions are non-overlapping polytopes in input space, each input sample belongs to a unique activation region, so inference with model f can be rewritten as $f(x) = h_i(x)$ where $x \in a_i$. For convenience we overload the definition of H so the subfunction induced for any input sample x is $H(x) \triangleq h_i$ where $x \in a_i$.

2.2 Smooth empirical error

Consider a training dataset S containing N sampled pairs, $S \in (\mathcal{X} \times \mathcal{Y})^N$, where samples are drawn iid from distribution D. Define the empirical error or risk of the full network on this dataset:

$$\widehat{R}_S(f) \triangleq \frac{1}{|S|} \sum_{n=1}^{|S|} r(S^n; f), \tag{2}$$

where r is a bounded error function on samples: $0 \leq r((x, y); f) \leq 1$ for all $x, y \in (\mathcal{X} \times \mathcal{Y})$ and S^n is the n-th element of S. Note empirical error, e.g. proportion of incorrect classifications, is not necessarily the objective function for training; it is fine for the latter to not have finite bounds. Quantify the empirical error for a subfunction h_i using standard empirical error (eq. (2)). The activation region dataset is $S_i \triangleq S \cap a_i$ with $N_i \triangleq |S_i|$ samples drawn iid from its data distribution D_i, defined as $\mathbb{P}_{D_i}(x, y) = \mathbb{P}_D(x, y | x \in a_i)$. Then:

$$\widehat{R}_{S_i}(h_i) = \frac{1}{N_i} \sum_{n=1}^{N_i} r(S_i^n; f), \tag{3}$$

$$\text{and for any } \delta \in (0, 1], \text{ with probability} > 1 - \delta: \qquad \mathop{\mathbb{E}}_{S_i}[\widehat{R}_{S_i}(h_i)] \leq \widehat{R}_{S_i}(h_i) + \sqrt{\frac{\log \frac{2}{\delta}}{2N_i}}. \tag{4}$$

This is a Hoeffding inequality based bound (Mohri et al., 2018, eq. 2.17). As we take a pre-trained model and rank test samples, the model is fixed. There are several drawbacks with this initial formulation. First, it treats the empirical error of different subfunctions as independent when in general, they are not. Since different activation regions are bounded by shared hyperplanes, and hence the subfunctions share parameters, there exists useful evidence for a subfunction's performance outside its own activation region. Second, test samples overwhelmingly induce unseen activation patterns in deep networks, and the bound in eq. (4) is infinite if $N_i = 0$, making this quantity uninformative for the purposes of comparing subfunctions.

This motivates the following empirical risk metric for subfunctions. Fix non-negative weighting or closeness distance function between subfunctions, $k : H \times H \to \mathcal{R}^{\geq 0}$. For any subfunction $h_i \in H$, define its probability mass:

$$\mathbb{P}(h_i) \triangleq \frac{\sum_{j\in[1,C]} N_j \; k(h_i, h_j)}{\sum_{l\in[1,C]} \sum_{j\in[1,C]} N_j \; k(h_l, h_j)}, \tag{5}$$

$$\text{so by construction} \sum_{i\in[1,C]} \mathbb{P}(h_i) = 1, \tag{6}$$

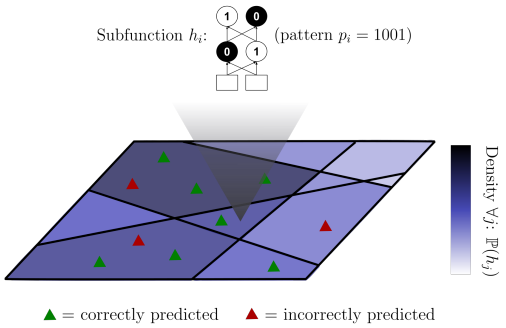

Figure 2: Each linear activation region in 2D input space (plane) is mapped to a unique subfunction, activation decision pattern, and set of training samples (triangles). A density, smooth in representation space, is defined given the number of samples in each region.

which quantifies how densely h_i is locally populated by training samples. Rewrite the empirical error of the network as an expectation over subfunction empirical error:

$$\widehat{R}_S(f) = \frac{1}{N} \sum_{(x,y)\in S} r((x,y); f) \tag{7}$$

$$= \frac{1}{N} \sum_{(x,y)\in S} \frac{1}{\sum_{j\in[1,C]} \mathbb{P}(h_j) \; k(H(x), h_j)} \sum_{i\in[1,C]} \mathbb{P}(h_i) \; k(H(x), h_i) \; r((x,y); f) \tag{8}$$

$$= \frac{1}{N} \sum_{i\in[1,C]} \mathbb{P}(h_i) \sum_{(x,y)\in S} \frac{k(H(x), h_i) \; r((x,y); f)}{\sum_{j\in[1,C]} \mathbb{P}(h_j) \; k(H(x), h_j)} \tag{9}$$

$$= \mathop{\mathbb{E}}_{h_i} \left[\frac{1}{N} \sum_{(x,y)\in S} \frac{k(H(x), h_i) \; r((x,y); f)}{\sum_{j\in[1,C]} \mathbb{P}(h_j) \; k(H(x), h_j)} \right] \tag{10}$$

$$= \mathop{\mathbb{E}}_{h_i} \left[\frac{1}{N} \sum_{l\in[1,C]} \frac{k(h_l, h_i) \; N_l \; \widehat{R}_{S_l}(h_l)}{\sum_{j\in[1,C]} \mathbb{P}(h_j) \; k(h_l, h_j)} \right] \triangleq \mathop{\mathbb{E}}_{h_i} [\widehat{R}^*_S(h_i)]. \tag{11}$$

Theorem 2.1 (Expected smooth error bound). *Assume that $\tilde{D}_S$ is a distribution over size-N datasets that have the same activation region data distributions and dataset sizes (D_i and N_i, $\forall i \in [1, C]$) as S. Let dataset S be drawn iid from $\tilde{D}_S$. Then $\forall i \in [1, C]$, for any given $\delta \in (0, 1]$, with probability $> 1 - \delta$:*

$$R^*_{\tilde{D}_S}(h_i) \triangleq \mathop{\mathbb{E}}_{S} [\widehat{R}^*_S(h_i)] \leq \widehat{R}^*_S(h_i) + \frac{1}{\mathbb{P}(h_i)} \sqrt{\frac{\log \frac{2}{\delta}}{2N}}, \tag{12}$$

proof in appendix A. Intuitively this implies that the more a subfunction is surrounded by samples for which the model makes accurate predictions - both from its own region and regions of other subfunctions, weighted by the weighting function k - the lower its empirical error and bound on generalization gap, and thus the lower its bound on true or expected error, given any δ. The further that test samples fall from densely supported training regions or subfunctions, the less likely the model is to be accurate. Unlike eq. (4), this bound is finite even for subfunctions without training samples because such subfunctions are assigned non-zero density (fig. 2), given a positive-valued weighting function.

Smoothing is performed out of necessity; in order to resolve the problem of not having empirical training samples to quantify the error of a subfunction, one must assume interdependence between subfunctions. In general, smoothing with k introduces a bias since the bound on a subfunction's smooth empirical error does not converge to expected error in the limit of number of samples of its region. However, smoothing is not unreasonable as errors of different subfunctions in neural networks are interdependent due to parameter sharing, and the bias is reducible by searching k, which experimental results indicate is sufficient to render it inconsequential in practice.

2.3 WEIGHTING FUNCTION

The bound in theorem 2.1 holds irrespective of choice of k because the bounding procedure assumes a worst case. This makes the bound loose, but allows for k to be searched using a validation set. In this section we discuss selecting k. The ideal weighting function k and probability parameter δ produce a bound for each subfunction h_i that reflects the subfunction's true error accurately, i.e. minimizes the difference with the expected true error (without weighting function) if we had unlimited samples of its activation region a_i:

$$\min_{k,\delta} \left\| \mathop{\mathbb{E}}_{S_i}[\widehat{R}_{S_i}(h_i)] - \left(\widehat{R}^*_S(h_i) + \frac{1}{\mathbb{P}(h_i)} \sqrt{\frac{\log \frac{2}{\delta}}{2N}} \right) \right\| \tag{13}$$

Being limited to dataset instance S, we do not have access to subfunction h_i's true error $\mathbb{E}_{S_i}[\widehat{R}_{S_i}(h_i)]$. However, we can construct an estimate by taking the samples x, y that k includes in the subfunction's smooth empirical error $\widehat{R}^*_S(h_i)$ (that is, all the training samples, for positive valued k) and adjusting their error values to reflect what they would be if the sample did belong to a_i. This improves on $\widehat{R}^*_S(h_i)$, the weighted error of surrounding activation regions, by transforming it into a weighted error of the target activation region a_i itself.

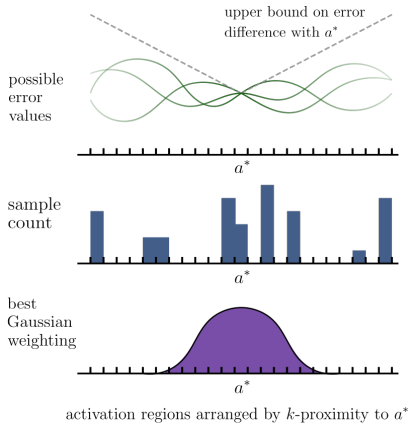

Figure 3: Given a family of Gaussian weighting functions, the best weighting function according to eq. (16) trades off precision of the smooth empirical error with sample density.

Let $\Phi : \mathcal{X} \to \mathcal{Z}$ be any data representation for which there exists a function $\Psi : \mathcal{Z} \to \mathbb{R}$ that computes inference model f's per-sample error, i.e. $r(x, y) = \Psi(\Phi(x))$ for all x, y in the support of D. This assumes the data is well conditioned so target labels are predictable from inputs. Let $\Omega : \mathcal{Z} \to \mathcal{Z}$ be a shifting function that changes the representation of any sample $x \in \mathcal{X}$ into the representation of a sample in a_i, $\Omega(\Phi(x)) \triangleq \arg\min_{\Phi(x')} \|\Phi(x') - \Phi(x)\|$ s.t. $x' \in a_i$. Using the Taylor expansion, assuming an error function Ψ with bounded first order gradients:

$$\forall (x, y) \in S : \Psi(\Omega(\Phi(x))) = \Psi(\Phi(x)) + \mathcal{O}(\|\Phi(x) - \Omega(\Phi(x))\|) \tag{14}$$

Replacing the true error in eq. (13) with the estimate constructed using shifted samples:

$$\left\| \frac{1}{N} \sum_{(x,y)\in S} \frac{1}{w(x)} k(H(x), h_i)\ \Psi(\Omega(\Phi(x))) - \left(\widehat{R}^*_S(h_i) + \frac{1}{\mathbb{P}(h_i)} \sqrt{\frac{\log \frac{2}{\delta}}{2N}} \right) \right\| \tag{15}$$

$$\leq \left\| \frac{1}{N} \sum_{(x,y)\in S} \frac{1}{w(x)} k(H(x), h_i)\ \mathcal{O}(\|\Phi(x) - \Omega(\Phi(x))\|) \right\| + \frac{1}{\mathbb{P}(h_i)} \sqrt{\frac{\log \frac{2}{\delta}}{2N}}, \tag{16}$$

where $w(x) \triangleq \sum_{j\in[1,C]} \mathbb{P}(h_j)\ k(H(x), h_j)$ is the weight normalization term. We draw 2 conclusions from this analysis. First, weighting value $k(h_i, h_j)$ for any h_i, h_j should decrease with the distance between the feature representations of samples in their activation regions. This is evident from eq. (16) as $\Phi(x)$ is the representation of a sample in the activation region of $H(x)$, and $\Omega(\Phi(x))$ is the representation of a sample in the activation region of h_i, so larger distances should be penalized by smaller weights. However, $k(h_i, h_j)$ cannot be too low (for example 0 for all $h_j \neq h_i$ given any h_i) because the magnitude of $\frac{1}{\mathbb{P}(h_i)}$ would be large. Thus the best k combines error precision (upweight near regions and downweight far regions) with support (upweight near and far regions). The need to minimize weight with distance justifies restricting the search for k within function classes where output decreases with representation distance, such as Gaussian functions of activation pattern distance. An example of this trade-off is illustrated in fig. 3.

Secondly, in practice there is no need to explicitly find k that minimizes eq. (16). A simple alternative is to use a validation set metric that correlates with how well k, δ minimize eq. (16) (i.e. approximate the true error), such as the ability of the bound to discriminate between validation samples that are accurately or inaccurately predicted, and select k and δ such that they minimize the validation metric. This is the approach we take in our experiments.

3 Related work

This work is primarily related to sample-level metrics intended for out-of-distribution or unreliable in-distribution sample selection (Ovadia et al., 2019), and work on linear activation regions, which is typically motivated by characterizing neural network expressivity (Montúfar et al., 2014; Raghu et al., 2017; Hanin & Rolnick, 2019).

Well known sample uncertainty or unreliability metrics include the maximum response of the final softmax prediction layer (Hendrycks & Gimpel, 2017; Geifman & El-Yaniv, 2017; Cordella et al., 1995; Chow, 1957), its entropy (Shannon, 1948), or its top-two margin (Scheffer et al., 2001), all conditioned on the input sample. Liang et al. (2017) combines maximum response with temperature scaling and input perturbations. Jiang et al. (2018) combines the top-two margin idea with class distance. Some ideas use distance to prototypes in representation space, which is similar at high level to ours if one assumes prototypes are in high-density regions. Lee et al. (2018) trains a logistic regressor on layer-wise distances of a sample's features to its nearest class, with the idea that distance to features of the nearest class should scale with unreliability. This was shown to outperform Liang et al. (2017). Sehwag et al. (2021) is an unsupervised variant of Lee et al. (2018). Tack et al. (2020) clusters feature representations instead of using classes, using distance to nearest cluster as unreliability. In Bergman & Hoshen (2020) the clusters are defined by input transformations; we were unable to get this working in our setting as models appear to suffer from feature collapse across transformations when not trained explicitly for transformation disentanglement. Non-parametric kernel based methods such as Gaussian processes provide measures of uncertainty that also scale with distance from samples and can be appended to a neural network base (Liu et al., 2020). Zhang et al. (2020) assume density in latent space is correlated to reliability, using residual flows (Chen et al., 2019) for the density model. If multiple models trained on the same dataset are available (which we do not assume), one could use ensemble model metrics such as variance, max response or entropy (Lakshminarayanan et al., 2016); an ensemble can also be simulated in a single model with Monte Carlo dropout (Geifman & El-Yaniv, 2017; Gal & Ghahramani, 2016).

Many of these works seek to predict whether a sample is out-of-distribution (OOD) for its own sake, which is an interesting problem, but we care about 1) epistemic uncertainty in general, including in-distribution misclassification, not just OOD 2) in the context of the main model trained for a practical task, or in other words, exposing what the task model does not know using the task model itself, as opposed to training separate models on the data distribution specifically for outlier detection.

4 Experiments

We tested the ability of the input-conditioned bound in eq. (12) to predict out-of-distribution and misclassified in-distribution samples. Taking pre-trained VGG16 and ResNet50 models for CIFAR100 and CIFAR10, we computed area under false positive rate vs. true positive rate (AUROC) and area under coverage vs. effective accuracy (AUCEA) for each method. Definitions are given in appendix E. These metrics treat predicting unreliable samples as a binary classification problem, where for out-of-distribution, ground truth is old distribution/new distribution, and for misclassified in-distribution, ground truth is classified correct/incorrect. Method output is accept/reject. All methods produce a metric per sample that is assumed to scale with unreliability, so 1K thresholds for discretizing into accept/reject decisions were uniformly sampled across the maximum test set range, yielding the AUROC and AUCEA curves. For our method, we used Gaussian weighting with standard deviation ρ, $k(h_i, h_j) = e^{-\text{Hamming}(p_i,p_j)^2/(2\rho^2)}$, and took log of the bound to suppress large magnitudes. In-distribution misclassification validation set was used to select all hyperparameters, i.e. we use a realistic, hard setting where OOD data is truly unseen for all parameters.

Table 1: Summary of out-of-distribution and misclassified in-distribution results, by difference to the top performing method in each architecture $\times$ dataset setting. Values are difference in AUROC and average $\pm$ standard deviation is shown over all architecture $\times$ dataset settings. Higher is better.

	Out-of-distr.	Misc. in-distr.	Average
Residual flows density (Chen et al., 2019)	-0.538 $\pm$ 2E-01	-0.356 $\pm$ 4E-02	-0.447 $\pm$ 1E-01
GP (Liu et al. (2020) w/ fixed features)	-0.204 $\pm$ 2E-01	-0.159 $\pm$ 1E-01	-0.181 $\pm$ 1E-01
Class distance (Lee et al., 2018)	-0.214 $\pm$ 1E-01	-0.334 $\pm$ 9E-02	-0.274 $\pm$ 1E-01
Margin (Scheffer et al., 2001)	-0.037 $\pm$ 2E-02	-0.007 $\pm$ 7E-03	-0.022 $\pm$ 1E-02
Entropy (Shannon, 1948)	-0.025 $\pm$ 2E-02	**-0.002 $\pm$ 2E-03**	-0.014 $\pm$ 1E-02
Max response (Cordella et al., 1995)	-0.034 $\pm$ 2E-02	-0.008 $\pm$ 8E-03	-0.021 $\pm$ 1E-02
MC dropout (Geifman & El-Yaniv, 2017)	-0.061 $\pm$ 3E-02	-0.048 $\pm$ 2E-02	-0.054 $\pm$ 2E-02
Cluster distance (Tack et al., 2020)	-0.052 $\pm$ 9E-02	-0.021 $\pm$ 7E-03	-0.036 $\pm$ 5E-02
Subfunctions (ours)	**-0.007 $\pm$ 1E-02**	-0.006 $\pm$ 4E-04	**-0.007 $\pm$ 6E-03**

Table 2: Results for models trained on CIFAR10 on out-of-distribution detection vs CIFAR100/SVHN. AUROC shown, higher is better. For equivalent table on CIFAR100, see table 5.

	→ CIFAR100		→ SVHN	
	VGG16	ResNet50	VGG16	ResNet50
Residual flows density	0.513 ± 2E-04	0.513 ± 1E-04	0.084 ± 1E-04	0.084 ± 1E-04
GP	0.810 ± 1E-02	0.575 ± 2E-02	0.844 ± 2E-02	0.473 ± 9E-02
Class distance	0.673 ± 7E-02	0.468 ± 3E-02	0.806 ± 6E-02	0.462 ± 1E-01
Margin	0.829 ± 2E-03	0.825 ± 5E-03	0.854 ± 4E-02	0.856 ± 2E-02
Entropy	0.853 ± 2E-03	0.822 ± 6E-03	0.869 ± 3E-02	0.858 ± 3E-02
Max response	0.829 ± 3E-03	0.827 ± 5E-03	0.850 ± 4E-02	0.858 ± 2E-02
MC dropout	0.776 ± 6E-03	0.807 ± 3E-03	0.778 ± 6E-02	0.838 ± 3E-02
Cluster distance	**0.862 ± 4E-03**	**0.867 ± 3E-03**	**0.870 ± 5E-02**	**0.892 ± 1E-02**
Subfunctions (ours)	**0.858 ± 4E-03**	**0.862 ± 2E-03**	**0.886 ± 2E-02**	**0.915 ± 2E-02**

We note 2 adjustments to the theory made in the practical experiments. First, for tractability on deep networks, we use a coarse partitioning of the network by taking activations from the last ReLU layer only, so the subfunctions are piecewise linear instead of purely linear. In this case activation regions are still disjoint, eq. (12) becomes a bound on piecewise linear subfunction error and still holds. Second, computing the set of feasible activation regions is intractable, so we use the full bit space, $P = \{0, 1\}^M$. This means the bound is computed in an altered subfunction space where some infeasible subfunctions are assigned a non-zero density, affecting the weight normalization. A benefit of using the full bit space is it allows computational savings when computing the bound, detailed in appendix B. These 2 limitations mean that the performance attained by the method in the experiments is a lower bound that is likely improvable if more tractable implementations are found.

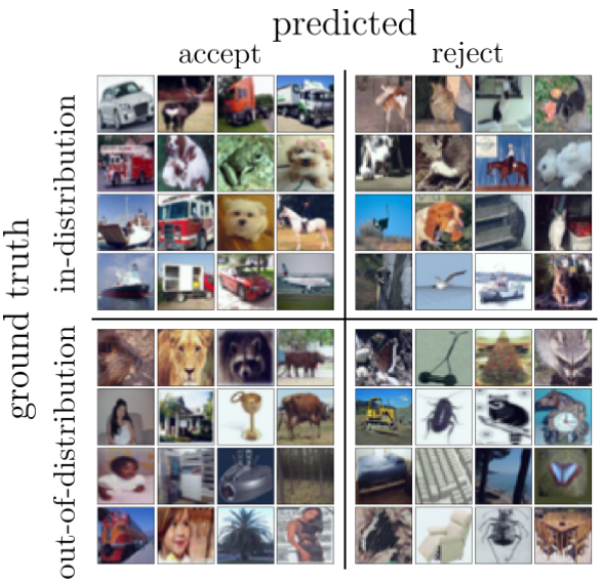

Figure 4: Sample confusion matrix, OOD for CIFAR10 → CIFAR100 on ResNet50. Random samples from top 20% in each quadrant shown.

Subfunctions and entropy were found to be the top 2 methods overall in each category (table 1), with subfunctions better on average. Cluster distance also performed well on CIFAR10, but was penalized by poor performance on CIFAR100 and particularly VGG16 (tables 5 and 6), which is a more difficult dataset for determining outlier status as the in-distribution classes are more finegrained. We conclude that subfunctions and entropy were good predictors of unreliability for both in-distribution and out-of-distribution scenarios. The AUCEA results for the in-distribution setting (tables 3 and 6) mean that using either to filter predictions would have raised effective model accuracy (accuracy of accepted samples) to $90 \sim 92\%$ from $70 \sim 73\%$ for the original CIFAR100 models, and to $98 \sim 99\%$ from $91 \sim 92\%$ for the original CIFAR10 models (table 4), on average over thresholds. Entropy is simpler and computationally cheaper than subfunction error bound, but suffers from the drawback that it can only be computed exactly if model inference includes a discrete probabilistic variable. This is the case for these experiments but not in general (e.g. consider MSE objectives), whereas our method does not have this restriction.

Empirically, we observed for subfunctions that reliable in-distribution images tended to be prototypical images for their class, whilst OOD images erroneously characterized as reliable tended to resemble the in-distribution classes, as one would expect (fig. 4). To test this hypothesis further, we took a CIFAR10 model and plotted the rankings of samples from each CIFAR100 class in fig. 5, where each box denotes the median and first and third quartiles. The classes are ordered by median. We identified the superclasses in CIFAR100 with the highest semantic overlap with CIFAR10 classes (made up of mostly vehicles and mammals), whose classes are coloured green. It is clear from the correlation between green and lower unreliability ranking that subfunction error bounds rate OOD classes semantically closer to the training classes as more reliable. Note that

Table 3: Results for models trained on CIFAR10. Predicting misclassification on in-distribution test. Higher is better. For equivalent table on CIFAR100, see table 6.

	VGG16		ResNet50	
	AUCEA	AUROC	AUCEA	AUROC
Residual flows density	0.442 ± 5E-02	0.520 ± 1E-02	0.492 ± 3E-02	0.577 ± 1E-02
GP	0.983 ± 1E-03	0.865 ± 8E-03	0.943 ± 5E-03	0.625 ± 2E-02
Class distance	0.948 ± 2E-02	0.669 ± 8E-02	0.900 ± 3E-02	0.471 ± 6E-02
Margin	0.982 ± 2E-03	0.900 ± 4E-03	0.848 ± 1E-02	**0.894 ± 4E-03**
Entropy	**0.989 ± 1E-04**	**0.914 ± 3E-03**	**0.984 ± 1E-03**	0.890 ± 5E-03
Max response	0.980 ± 3E-03	0.898 ± 4E-03	0.832 ± 1E-02	**0.895 ± 5E-03**
MC dropout	0.982 ± 6E-04	0.845 ± 6E-03	0.976 ± 2E-03	0.868 ± 1E-02
Cluster distance	0.988 ± 4E-04	0.901 ± 2E-03	0.981 ± 2E-03	0.867 ± 2E-03
Subfunctions (ours)	**0.988 ± 3E-04**	**0.907 ± 3E-03**	**0.983 ± 2E-03**	0.889 ± 6E-03

even the exceptions towards the right are justified, because the inclusion of e.g. bicycles, lawn mowers and rockets in "vehicles" is questionable; certainly these objects do not correspond visually to the vehicle classes in CIFAR10. In addition, we ran the same plot for the other methods and found that in every case the correlation between reliability and semantic familiarity was less strong (appendix G).

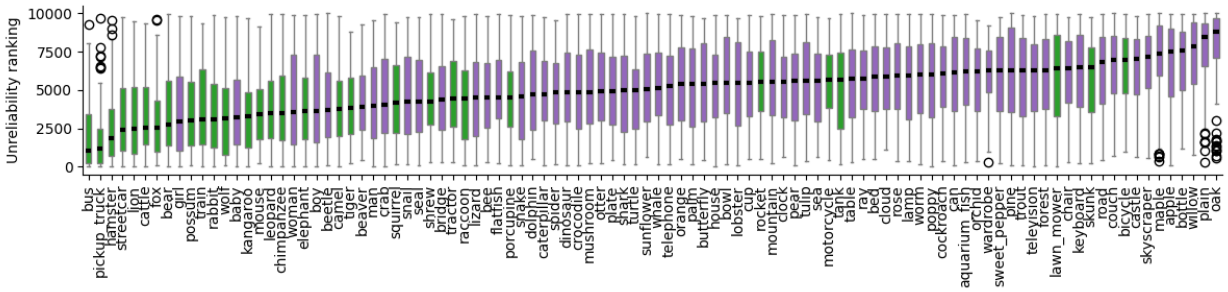

Figure 5: OOD for CIFAR10 → CIFAR100 on ResNet50. 10k CIFAR100 test samples were ranked by unreliability (log STEB). Boxplots summarize rankings per class (lower = less unreliable). Green denotes superclasses similar to CIFAR10: carnivores, omnivores, herbivores, mammals, vehicles.

5 Conclusion

Density of training samples in representation space appears to be a feasible indicator of reliability of predictions for trained piecewise linear neural networks. This raises several interesting questions for future work:

- Measures of unreliability that scale with density of continuous input samples in representation space, rather than density of discrete partitions, which is specialized to piecewise linear neural networks.
- Deriving tighter bounds, for example by making stronger assumptions about the weighting function k used.
- Implications for model selection; how to train networks such that samples fall in high-density regions in representation space.

With regards to model selection, a reasonable hypothesis based on our results is that generalization ability of neural networks scales with the proportion of test inputs mapped to high-density regions in its representation space. Low-density activation regions are less likely in compact representation spaces, all else equal, since the same number of training samples is distributed over fewer representations. This is an intuition rather than a formal result of this work, but it links to a body of work on the relation between compact representation spaces and generalization. Compactness is optimized for in information bottlenecks (Tishby et al., 2000; Ahuja et al., 2021), which minimize the entropy of network representations, and implicitly by sparse factor graphs (Goyal & Bengio, 2020) and feature discretization methods (Liu et al., 2021; Van Den Oord et al., 2017) including discrete output unsupervised learning (Ji et al., 2019), which are methods that build low expressivity into the model as a prior for improved generalization. We conclude that learning compact representation spaces with few, densely supported modes is an interesting direction for future work on neural network generalization.

REFERENCES

Kartik Ahuja, Ethan Caballero, Dinghuai Zhang, Yoshua Bengio, Ioannis Mitliagkas, and Irina Rish. Invariance principle meets information bottleneck for out-of-distribution generalization. *arXiv preprint arXiv:2106.06607*, 2021.

Liron Bergman and Yedid Hoshen. Classification-based anomaly detection for general data. *arXiv preprint arXiv:2005.02359*, 2020.

Ricky TQ Chen, Jens Behrmann, David Duvenaud, and Jörn-Henrik Jacobsen. Residual flows for invertible generative modeling. *arXiv preprint arXiv:1906.02735*, 2019.

Chi-Keung Chow. An optimum character recognition system using decision functions. *IRE Transactions on Electronic Computers*, pp. 247–254, 1957.

Luigi Pietro Cordella, Claudio De Stefano, Francesco Tortorella, and Mario Vento. A method for improving classification reliability of multilayer perceptrons. *IEEE Transactions on Neural Networks*, 6(5):1140–1147, 1995.

Yarin Gal and Zoubin Ghahramani. Dropout as a Bayesian approximation: Representing model uncertainty in deep learning. In *international conference on machine learning*, pp. 1050–1059. PMLR, 2016.

Yonatan Geifman and Ran El-Yaniv. Selective classification for deep neural networks. *arXiv preprint arXiv:1705.08500*, 2017.

Anirudh Goyal and Yoshua Bengio. Inductive biases for deep learning of higher-level cognition. *arXiv preprint arXiv:2011.15091*, 2020.

Boris Hanin and David Rolnick. Deep ReLU networks have surprisingly few activation patterns. *Advances in Neural Information Processing Systems*, 32:361–370, 2019.

Dan Hendrycks and Kevin Gimpel. A baseline for detecting misclassified and out-of-distribution examples in neural networks. In *ICLR*, 2017.

Xu Ji, Joao F Henriques, and Andrea Vedaldi. Invariant information clustering for unsupervised image classification and segmentation. In *Proceedings of the IEEE/CVF International Conference on Computer Vision*, pp. 9865–9874, 2019.

Heinrich Jiang, Been Kim, Melody Y Guan, and Maya R Gupta. To trust or not to trust a classifier. In *NeurIPS*, pp. 5546–5557, 2018.

Alex Krizhevsky. Learning multiple layers of features from tiny images. 2009.

Balaji Lakshminarayanan, Alexander Pritzel, and Charles Blundell. Simple and scalable predictive uncertainty estimation using deep ensembles. *arXiv preprint arXiv:1612.01474*, 2016.

Kimin Lee, Kibok Lee, Honglak Lee, and Jinwoo Shin. A simple unified framework for detecting out-of-distribution samples and adversarial attacks. *arXiv preprint arXiv:1807.03888*, 2018.

Shiyu Liang, Yixuan Li, and Rayadurgam Srikant. Enhancing the reliability of out-of-distribution image detection in neural networks. *arXiv preprint arXiv:1706.02690*, 2017.

Dianbo Liu, Alex Lamb, Kenji Kawaguchi, Anirudh Goyal, Chen Sun, Michael Curtis Mozer, and Yoshua Bengio. Discrete-valued neural communication. *arXiv preprint arXiv:2107.02367*, 2021.

Jeremiah Zhe Liu, Zi Lin, Shreyas Padhy, Dustin Tran, Tania Bedrax-Weiss, and Balaji Lakshminarayanan. Simple and principled uncertainty estimation with deterministic deep learning via distance awareness. *arXiv preprint arXiv:2006.10108*, 2020.

Mehryar Mohri, Afshin Rostamizadeh, and Ameet Talwalkar. *Foundations of machine learning*. MIT press, 2018.

Guido Montúfar, Razvan Pascanu, Kyunghyun Cho, and Yoshua Bengio. On the number of linear regions of deep neural networks. *arXiv preprint arXiv:1402.1869*, 2014.

Yuval Netzer, Tao Wang, Adam Coates, Alessandro Bissacco, Bo Wu, and Andrew Y Ng. Reading digits in natural images with unsupervised feature learning. 2011.

Yaniv Ovadia, Emily Fertig, Jie Ren, Zachary Nado, David Sculley, Sebastian Nowozin, Joshua V Dillon, Balaji Lakshminarayanan, and Jasper Snoek. Can you trust your model's uncertainty? Evaluating predictive uncertainty under dataset shift. *arXiv preprint arXiv:1906.02530*, 2019.

Maithra Raghu, Ben Poole, Jon Kleinberg, Surya Ganguli, and Jascha Sohl-Dickstein. On the expressive power of deep neural networks. In *international conference on machine learning*, pp. 2847–2854. PMLR, 2017.

Carl Edward Rasmussen. Gaussian processes in machine learning. In *Summer school on machine learning*, pp. 63–71. Springer, 2003.

Tobias Scheffer, Christian Decomain, and Stefan Wrobel. Active hidden markov models for information extraction. In *International Symposium on Intelligent Data Analysis*, pp. 309–318. Springer, 2001.

Vikash Sehwag, Mung Chiang, and Prateek Mittal. Ssd: A unified framework for self-supervised outlier detection. *arXiv preprint arXiv:2103.12051*, 2021.

Claude E Shannon. A mathematical theory of communication. *The Bell system technical journal*, 27(3):379–423, 1948.

Jihoon Tack, Sangwoo Mo, Jongheon Jeong, and Jinwoo Shin. Csi: Novelty detection via contrastive learning on distributionally shifted instances. *arXiv preprint arXiv:2007.08176*, 2020.

Naftali Tishby, Fernando C Pereira, and William Bialek. The information bottleneck method. *arXiv preprint physics/0004057*, 2000.

Aaron Van Den Oord, Oriol Vinyals, et al. Neural discrete representation learning. *Advances in neural information processing systems*, 30, 2017.

Hongjie Zhang, Ang Li, Jie Guo, and Yanwen Guo. Hybrid models for open set recognition. In *European Conference on Computer Vision*, pp. 102–117. Springer, 2020.

A PROOF FOR THEOREM 2.1

This follows the Chernoff/Hoeffding bounding technique. Fix model f, patterns P and thus subfunctions set H. Let the true data distribution for each activation region a_i be D_i. Assume that $\tilde{D}_S$ is a distribution over size-N datasets that have the same activation region data distributions and dataset sizes (D_i and $N_i, \forall i \in [1, C]$) as S. Consider S as a dataset drawn iid from $\tilde{D}_S$. Without loss of generality, since dataset order is immaterial for the error metrics, assume the index n of sample S^n determines its activation region and distribution from which it is drawn independently of other samples. That is, $\forall n \in [1, N] : S^n \sim D_{J^n}$ iid for some fixed $J \in [1, C]^N$. Recall that D_i is constructed as $\mathbb{P}_{D_i}(x, y) = \mathbb{P}_D(x, y | x \in a_i)$. Call the inputs and targets X_S and Y_S, $\forall n \in [1, N] : (X_S^n, Y_S^n) \triangleq S^n$. Recall that empirical error function for samples is bounded: $\forall x, y \in (\mathcal{X} \times \mathcal{Y}) : 0 \leq r((x, y); f) \leq 1$ and weighting function k is non-negative valued.

Choose any subfunction $h_i \in H, i \in [1, C]$. Then $\forall \epsilon > 0, t > 0, \tilde{S} \sim \tilde{D}_S$ iid:

$$\mathop{\mathbb{P}}_{S}(\widehat{R}^*_S(h_i) - R^*_{\tilde{D}_S}(h_i) \geq \epsilon) = \mathop{\mathbb{P}}_{S}(\widehat{R}^*_S(h_i) - \mathop{\mathbb{E}}_{\tilde{S}}[\widehat{R}^*_{\tilde{S}}(h_i)] \geq \epsilon) \tag{17}$$

$$= \mathop{\mathbb{P}}_{S}(e^{t(\widehat{R}^*_S(h_i) - \mathbb{E}_{\tilde{S}}[\widehat{R}^*_{\tilde{S}}(h_i)])} \geq e^{t\epsilon}) \tag{18}$$

$$\leq e^{-t\epsilon} \mathop{\mathbb{E}}_{S}[e^{t(\widehat{R}^*_S(h_i) - \mathbb{E}_{\tilde{S}}[\widehat{R}^*_{\tilde{S}}(h_i)])}] \tag{19}$$

$$= e^{-t\epsilon} \mathop{\mathbb{E}}_{S}[e^{t \sum_{n=1}^{N} \left(\frac{k(H(X_S^n), h_i)\ r(S^n; f)}{N \sum_{j \in [1,C]} \mathbb{P}(h_j)\ k(H(X_S^n), h_j)} - \mathbb{E}_{\tilde{S}^n} \left[\frac{k(H(X_{\tilde{S}}^n), h_i)\ r(\tilde{S}^n; f)}{N \sum_{j \in [1,C]} \mathbb{P}(h_j)\ k(H(X_{\tilde{S}}^n), h_j)} \right] \right)}] \tag{20}$$

$$= e^{-t\epsilon} \prod_{n=1}^{N} \mathop{\mathbb{E}}_{S^n}[e^{t \left(\frac{k(H(X_S^n), h_i)\ r(S^n; f)}{N \sum_{j \in [1,C]} \mathbb{P}(h_j)\ k(H(X_S^n), h_j)} - \mathbb{E}_{\tilde{S}^n} \left[\frac{k(H(X_{\tilde{S}}^n), h_i)\ r(\tilde{S}^n; f)}{N \sum_{j \in [1,C]} \mathbb{P}(h_j)\ k(H(X_{\tilde{S}}^n), h_j)} \right] \right)}] \tag{21}$$

$$\leq e^{-t\epsilon} \prod_{n=1}^{N} e^{\frac{t^2 \left(\frac{1}{N\, \mathbb{P}(h_i)} - 0 \right)^2}{8}} \tag{22}$$

$$= e^{\frac{t^2}{8N\, \mathbb{P}(h_i)^2} - t\epsilon}, \tag{23}$$

by making use of the following:

1. eq. (18) $\rightarrow$ eq. (19) : Markov's inequality. For random variable $Z \geq 0$ and constant $a > 0$, $\mathbb{P}(Z \geq a) \leq \frac{\mathbb{E}[Z]}{a}$.
2. eq. (19) $\rightarrow$ eq. (20) : definition of $\widehat{R}^*_S(h_i)$ and linearity of expectation.
3. eq. (20) $\rightarrow$ eq. (21) : $\widehat{R}^*_S(h_i)$ is a sum over independently drawn samples. $\forall h_j \in H : \mathbb{P}(h_j)$ is constant because activation region dataset sizes are constant.
4. eq. (21) $\rightarrow$ eq. (22) : first bound the length of the range of the exponent. $\forall i \in [1, C], n \in [1, N] : 0 \leq \frac{k(H(X_S^n), h_i)\ r(S^n; f)}{N \sum_{j \in [1,C]} \mathbb{P}(h_j)\ k(H(X_S^n), h_j)} \leq \frac{k(H(X_S^n), h_i)}{N\, \mathbb{P}(h_i)\ k(H(X_S^n), h_i)} = \frac{1}{N\, \mathbb{P}(h_i)}$. Subtracting a constant does not change the length of the range of a random variable. Then apply Hoeffding's lemma: for random variable Z where $a \leq Z \leq b$ and $\mathbb{E}[Z] = 0$, then $\forall t > 0 : \mathbb{E}[e^{tZ}] \leq e^{\frac{t^2 (b-a)^2}{8}}$ holds.

Find the optimal t as the one that yields the tightest bound:

$$\nabla_t e^{\frac{t^2}{8N\, \mathbb{P}(h_i)^2} - t\epsilon} = 0, \qquad t = 4N\epsilon\, \mathbb{P}(h_i)^2, \tag{24}$$

which is a minimum because the second derivative is positive. Substitute into eq. (23) :

$$\mathop{\mathbb{P}}_{S}(\widehat{R}^*_S(h_i) - R^*_{\tilde{D}_S}(h_i) \geq \epsilon) \leq e^{-2N\epsilon^2\, \mathbb{P}(h_i)^2}. \tag{25}$$

The symmetric case can be proved in the same way:

$$\mathop{\mathbb{P}}_{S}(\widehat{R}^*_S(h_i) - R^*_{\tilde{D}_S}(h_i) \leq -\epsilon) = \mathop{\mathbb{P}}_{S}(R^*_{\tilde{D}_S}(h_i) - \widehat{R}^*_S(h_i) \geq \epsilon) \leq e^{-2N\epsilon^2\, \mathbb{P}(h_i)^2}, \tag{26}$$

specifically because swapping the order of the subtraction in eq. (21) does not change the value of the squared range used in eq. (22). Combining eq. (25) and eq. (26):

$$\mathop{\mathbb{P}}_{S}(|\widehat{R}^*_S(h_i) - R^*_{\tilde{D}_S}(h_i)| \geq \epsilon) \leq 2e^{-2N\epsilon^2\, \mathbb{P}(h_i)^2}. \tag{27}$$

Setting the right hand side to δ and solving for ϵ completes the derivation. Namely for any $\delta > 0$, the following hold with probability $\leq \delta$:

$$|\widehat{R}^*_S(h_i) - R^*_{\tilde{D}_S}(h_i)| \geq \frac{1}{\mathbb{P}(h_i)} \sqrt{\frac{\log \frac{2}{\delta}}{2N}} \tag{28}$$

$$R^*_{\tilde{D}_S}(h_i) - \widehat{R}^*_S(h_i) \geq \frac{1}{\mathbb{P}(h_i)} \sqrt{\frac{\log \frac{2}{\delta}}{2N}}. \tag{29}$$

Hence the following hold with probability $> 1 - \delta$:

$$R^*_{\tilde{D}_S}(h_i) < \widehat{R}^*_S(h_i) + \frac{1}{\mathbb{P}(h_i)} \sqrt{\frac{\log \frac{2}{\delta}}{2N}} \tag{30}$$

$$R^*_{\tilde{D}_S}(h_i) \leq \widehat{R}^*_S(h_i) + \frac{1}{\mathbb{P}(h_i)} \sqrt{\frac{\log \frac{2}{\delta}}{2N}}. \tag{31}$$

□.

B EFFICIENT COMPUTATION OF BOUND

For normalization in eq. (5), we reduce computational complexity from exponential $\mathcal{O}(N2^M)$ to linear $\mathcal{O}(M)$ (derivations below):

$$\sum_{l \in [1,C]} \sum_{\substack{j \in [1,C] \\ \text{s.t. } N_j > 0}} N_j \; k(h_l, h_j) = N \sum_{b=0}^{M} d(b) \binom{M}{b} \triangleq u, \tag{32}$$

and for normalization in eq. (11), from exponential $\mathcal{O}(N^2 2^M)$ to polynomial $\mathcal{O}(N^2 + M^3)$:

$$\forall_{\substack{l \in [1,C] \\ \text{s.t. } N_l > 0}} : \sum_{j \in [1,C]} \mathbb{P}(h_j) \; k(h_l, h_j) = \frac{1}{u} \sum_{\substack{i \in [1,C] \\ \text{s.t. } N_i > 0}} N_i \; z(\text{Hamming}(p_l, p_i)), \tag{33}$$

$$\text{where } \forall a \in [0, M] : z(a) \triangleq \sum_{b=0}^{M} d(b) \sum_{c=0}^{b} \binom{a}{c} \binom{M-a}{b-c} \; d(a + (b - c) - c). \tag{34}$$

Normalization term in eq. (5). Computed once for the network.

$$\sum_{l \in [1,C]} \sum_{\substack{j \in [1,C] \\ \text{s.t. } N_j > 0}} N_j \; k(h_l, h_j) = \sum_{\substack{j \in [1,C] \\ \text{s.t. } N_j > 0}} N_j \sum_{l \in [1,C]} k(h_l, h_j) = N \sum_{b=0}^{M} d(b) \binom{M}{b} \triangleq u, \tag{35}$$

where the trick is that $\sum_{l \in [1,C]} k(h_l, h_j) = \sum_{l \in [1,C]} d(\text{Hamming}(p_l, p_j))$ is the same for all h_j due to completeness of the bit space P, and the specific value can be found by looping through all possible Hamming distances b. This reduces the computational complexity from $\mathcal{O}(N2^M)$ to $\mathcal{O}(M)$, because the number of populated activation regions, i.e. length of loop over j, is upper bounded by the number of samples N, and $\binom{M}{b}$ can be iteratively updated in $\mathcal{O}(1)$ in the loop over b:

$$\binom{M}{b} = \binom{M}{b-1} \frac{M - (b-1)}{b}. \tag{36}$$

Normalization term in eq. (11). Computed $\forall l \in [1, C]$ s.t. $N_l > 0$:

$$\sum_{j\in[1,C]} \mathbb{P}(h_j)\; k(h_l, h_j) \tag{37}$$

$$= \frac{1}{u} \sum_{j\in[1,C]} \sum_{\substack{i\in[1,C] \\ \text{s.t. } N_i>0}} k(h_l, h_j)\; k(h_j, h_i)\; N_i \tag{38}$$

$$= \frac{1}{u} \sum_{\substack{i\in[1,C] \\ \text{s.t. } N_i>0}} N_i \sum_{j\in[1,C]} k(h_l, h_j)\; k(h_j, h_i) \tag{39}$$

$$= \frac{1}{u} \sum_{\substack{i\in[1,C] \\ \text{s.t. } N_i>0}} N_i \overbrace{\sum_{b=0}^{M} \overbrace{d(b)}^{\text{from } k(h_l,h_j)} \sum_{c=0}^{b} \binom{\text{Hamming}(p_l,p_i)}{c} \binom{M-\text{Hamming}(p_l,p_i)}{b-c}}^{=z(\text{Hamming}(p_l,p_i))\text{ (eq. (34))}} \cdot \overbrace{d(\text{Hamming}(p_l,p_i)+(b-c)-c)}^{\text{from } k(h_j,h_i)}. \tag{40}$$

Note the loops over i and l only need to range over populated activation regions due to the inclusion of their sample counts (N_i and N_l) as multiplicative factors in their loop contents, which means the iterations are bounded by $\mathcal{O}(N)$. The problematic loop is over j, i.e. all subfunctions/activation regions whether populated by samples or not, which is $\mathcal{O}(2^M)$ when P is the full bit space $\{0,1\}^M$. However, similar to eq. (35) above, it is also this fullness that we exploit.

Now we explain eq. (40) in detail. The value $z(\text{Hamming}(p_l, p_i))$ corresponds to the sum over j in eq. (39): loop over every bit pattern p_j in P, multiply its closeness to p_l with its closeness to p_i (both fixed outside this loop), and sum. Now group p_j by bit distance to p_l, b. Consider one instance of b (fig. 6). Within this group for b, the closeness of every p_j to p_l is constant, namely equal to $d(b)$. But they have different distances to p_i. However we know the number of bits that are different between p_l and p_i: this is $\text{Hamming}(p_l, p_i)$. Consider a specific instance of p_j. Visualize p_l turning into p_j by flipping bit one at a time; each will either bring the pattern closer to or further away from p_i. There is a budget of b different bits to flip to reach p_j. Say c of those flips brought it closer (i.e. turned the bit value at that position into the same as p_i's). Then we know $b-c$ brought it further. So the number of different bits between p_j and p_i is exactly $\text{Hamming}(p_l, p_i) + (b-c) - c$. And the number of p_j that fit this description is the number of ways of choosing c from the different bits between p_l and p_i multiplied by the number of ways of choosing $b-c$ from the shared bits between p_l and p_i: $\binom{\text{Hamming}(p_l,p_i)}{c}\binom{M-\text{Hamming}(p_l,p_i)}{b-c}$.

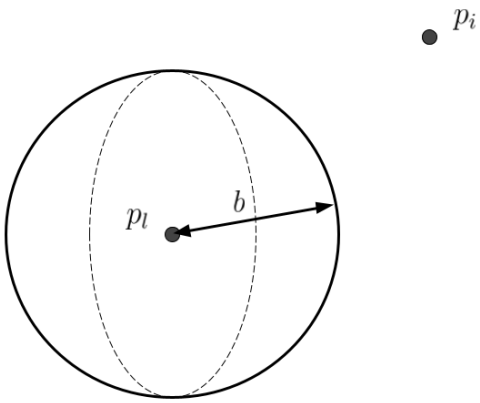

Figure 6: Sphere of p_j that are b bits away from p_l. For illustration only.

Conveniently, $\binom{q}{g} = 0$ for $g > q$, so there is no need to add special cases to exclude the cases where the number we seek to choose is greater than the number available.

Equation (40) enables computational complexity reduction of eq. (38), including the outer loop over l, from exponential to polynomial time: $\mathcal{O}(N^2 2^M)$ to $\mathcal{O}(N^2 + M^3)$ (excluding computation of u). The M^3 comes from constructing lookup table z, with the cubed power coming from looping over all possible values for $\text{Hamming}(p_l, p_i)$, b and c. This subsumes M^2 to compute $\forall q \in [0, M], \forall g \in [0, M] : \binom{q}{g}$ in the same iterative manner as eq. (36).

C PSEUDO-CODE

Algorithm 1: Subfunction error bounds for predicting sample prediction unreliability

Require: pre-trained model f_θ and training/validation/test datasets.
Compute activation patterns for training and validation data from last ReLU layer;
for hyperparameter values δ, ρ **do**
    Compute global normalization constant (eq. (32));
    For training data activation patterns, compute normalization constants (eq. (33));
    For validation data activation patterns, compute log bound using δ, ρ and normalization constants (eq. (12));
    Compute validation metric (AUCEA) with log bound of sample's activation pattern as unreliability;
    if highest validation metric **then**
        Store δ, ρ as best with normalization constants;
    end
end
Compute activation patterns for test data from last ReLU layer;
For test data activation patterns, compute log bound using chosen δ, ρ and normalization constants (eq. (12));
Compute test metrics with log bound of sample's activation pattern as unreliability.

D ADDITIONAL RESULTS TABLES

Table 4: Test accuracy of original models.

Dataset	Model	Accuracy
CIFAR100	VGG16	0.704 ± 1E-03
CIFAR100	ResNet50	0.729 ± 8E-03
CIFAR10	VGG16	0.920 ± 2E-03
CIFAR10	ResNet50	0.908 ± 5E-03

Table 5: Model trained on CIFAR100. Out-of-distribution detection (AUROC) vs CIFAR10/SVHN.

	→ CIFAR10		→ SVHN	
	VGG16	ResNet50	VGG16	ResNet50
Residual flows density	0.495 ± 2E-04	0.495 ± 2E-04	0.090 ± 2E-04	0.090 ± 2E-04
GP	0.708 ± 6E-03	0.404 ± 3E-02	**0.830 ± 3E-02**	0.396 ± 8E-02
Class distance	0.627 ± 4E-02	0.513 ± 4E-02	**0.833 ± 3E-02**	0.579 ± 1E-01
Margin	0.716 ± 2E-03	0.736 ± 3E-03	0.771 ± 5E-03	0.790 ± 3E-02
Entropy	**0.725 ± 3E-03**	0.745 ± 3E-03	0.786 ± 6E-03	**0.814 ± 4E-02**
Max response	0.719 ± 3E-03	0.740 ± 3E-03	0.776 ± 6E-03	0.799 ± 3E-02
MC dropout	0.693 ± 3E-03	0.725 ± 4E-03	0.771 ± 1E-02	0.795 ± 3E-02
Cluster distance	0.639 ± 1E-02	**0.754 ± 4E-03**	0.561 ± 2E-02	**0.810 ± 5E-02**
Subfunctions (ours)	**0.738 ± 2E-03**	**0.750 ± 7E-03**	0.797 ± 8E-03	0.807 ± 3E-02

Table 6: Model trained on CIFAR100. Predicting misclassification on in-distribution test (AUCEA and AUROC).

	VGG16		ResNet50	
	AUCEA	AUROC	AUCEA	AUROC
Residual flows density	0.293 ± 1E-02	0.622 ± 1E-02	0.293 ± 2E-02	0.630 ± 1E-02
GP	0.882 ± 1E-03	0.803 ± 2E-03	0.670 ± 2E-02	0.384 ± 2E-02
Class distance	0.838 ± 3E-02	0.739 ± 6E-02	0.627 ± 7E-02	0.476 ± 3E-02
Margin	0.899 ± 2E-03	0.852 ± 4E-03	0.870 ± 6E-03	0.855 ± 4E-03
Entropy	0.895 ± 2E-03	**0.856 ± 5E-03**	**0.916 ± 4E-03**	**0.859 ± 4E-03**
Max response	**0.899 ± 2E-03**	0.853 ± 4E-03	0.864 ± 7E-03	**0.857 ± 4E-03**
MC dropout	0.894 ± 1E-03	0.828 ± 8E-03	0.898 ± 5E-03	0.841 ± 2E-03
Cluster distance	0.833 ± 9E-03	0.722 ± 2E-02	0.900 ± 5E-03	0.824 ± 7E-03
Subfunctions (ours)	**0.904 ± 1E-03**	**0.864 ± 3E-03**	**0.902 ± 4E-03**	0.827 ± 4E-03

E METRICS

Evaluation metrics were area under the graphs of coverage vs. effective accuracy (AUCEA) and false positive rate vs. true positive rate (AUROC), with the latter as standard for OOD experiments.

$$\text{coverage} = \frac{TP + FP}{TP + FP + TN + FN} \qquad \text{effective accuracy} = \text{precision} = \frac{TP}{TP + FP} \tag{41}$$

$$\text{false positive rate} = \frac{FP}{FP + TN} \qquad \text{true positive rate} = \frac{TP}{TP + FN}. \tag{42}$$

F ADDITIONAL EXPERIMENTAL DETAILS

Experiments were averaged over 5 random seeds. The classification models were trained with SGD optimization with learning rate 0.1, momentum 0.9, weight decay 5e-4 and standard schedules: 100 epochs with learning rate $^*0.1$ every 30 epochs (CIFAR10) and 200 epochs with learning rate $^*0.2$ every 60 epochs (CIFAR100). For each unreliability metric, each threshold yielded one set of accept/reject decisions for the test set which yielded one point in each evaluation graph, and area under graph was computed using the trapezoidal rule. For the in-distribution setting, AUCEA corresponds to effective model accuracy (i.e. of accepted samples) averaged over different thresholds, and thus can be compared against original model accuracy.

F.1 SUBFUNCTION ERROR BOUND HYPERPARAMETERS

The searched values for likelihood parameter δ were [0.001, 0.01, 0.1, 0.2, 0.3, 0.4, 0.5, 0.6, 0.7, 0.8, 0.9] and for weighting function standard deviation parameter ρ were [32, 48, 64, 98, 128, 192, 256, 384, 512] (VGG16) and [4, 6, 8, 12, 16, 24, 32, 48, 64] (ResNet50). Validation set AUCEA was used for selection. The selected values are in table 7.

Table 7: Hyperparameters used for subfunction error. Brackets denote number of seeds.

Dataset	Model	ρ	δ
CIFAR100	VGG16	128.0 (#: 5)	0.001 (#: 5)
CIFAR100	ResNet50	16.0 (#: 5)	0.001 (#: 4), 0.1 (#: 1)
CIFAR10	VGG16	48.0 (#: 3), 98.0 (#: 1), 64.0 (#: 1)	0.001 (#: 4), 0.9 (#: 1)
CIFAR10	ResNet50	16.0 (#: 3), 24.0 (#: 2)	0.001 (#: 4), 0.3 (#: 1)

F.2 DATASET STATISTICS

All results infer unreliability of the test sets. The datasets are publicly available.

Dataset	Train	Validation	Test
CIFAR10 (Krizhevsky, 2009)	42500	7500	10000
CIFAR100 (Krizhevsky, 2009)	42500	7500	10000
SVHN (Netzer et al., 2011)	62269	10988	26032

F.3 Computational resources

Experiments were run given a shared cluster of machines with approximately 140 GPUs. Jobs required less than 24GB GPU memory. For subfunction error, normalization constants were computed first in a pre-computation phase. This took up most of the runtime and was parallelized by splitting jobs by architecture, dataset, seed and ρ; each job took approximately 20 minutes. Subsequent inference on the test sets (i.e. computing unreliability of unseen samples) took approximately 2 - 10 minutes per combination of architecture, dataset and seed.

G Additional Boxplots for other methods

Settings apart from the method are the same as fig. 5. We measured the Spearman correlation coefficient between semantic novelty (green=0, purple=1) and unreliability (median unreliability rank for each class) and found the correlation was lower for all baselines compared to subfunctions, which had a correlation coefficient of 0.511. The closest baseline method was MC dropout (table 8).

Table 8: Pearson correlation coefficients between unreliability rank and semantic novelty w.r.t. CIFAR10, on CIFAR100 data and CIFAR10 model. Higher is better.

Method	Correlation
Residual flows density	-0.259
GP	0.390
Class distance	0.171
Margin	0.231
Entropy	0.252
Max response	0.242
MC dropout	0.433
Cluster distance	0.347
Subfunctions (ours)	**0.511**

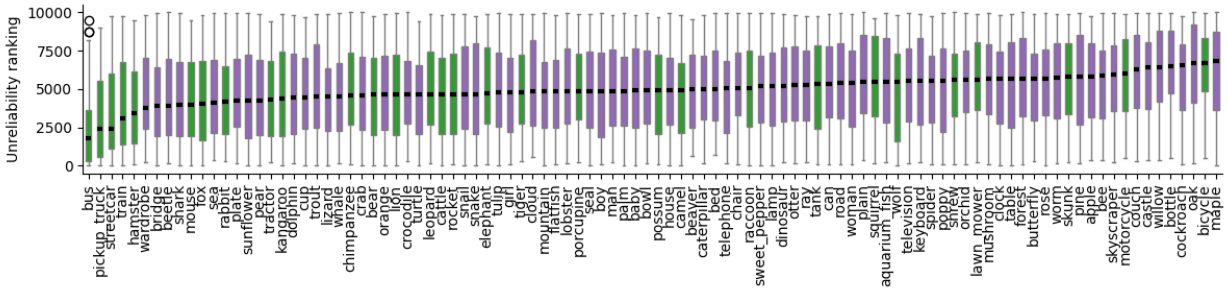

Figure 7: Entropy.

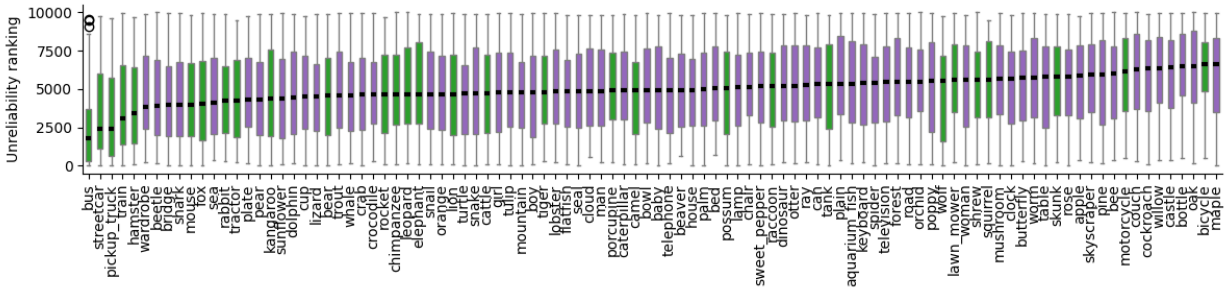

Figure 8: Max response.

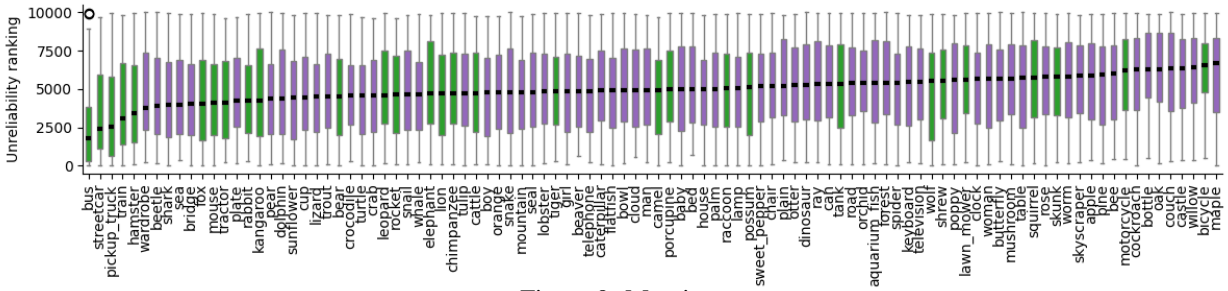

Figure 9: Margin.

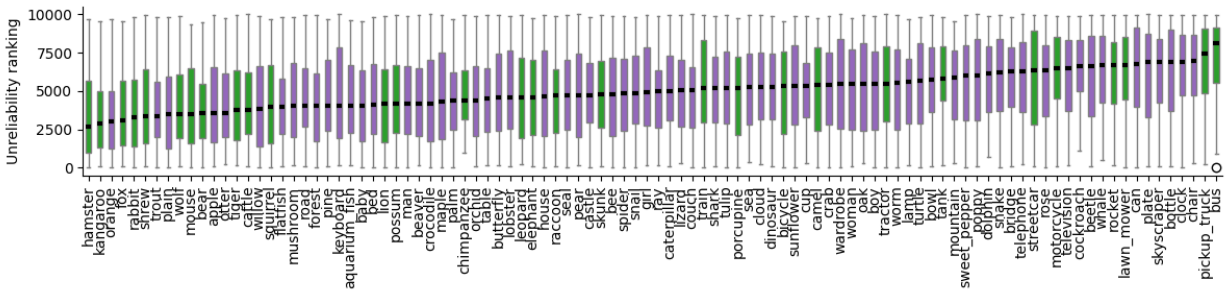

Figure 10: Class distance.

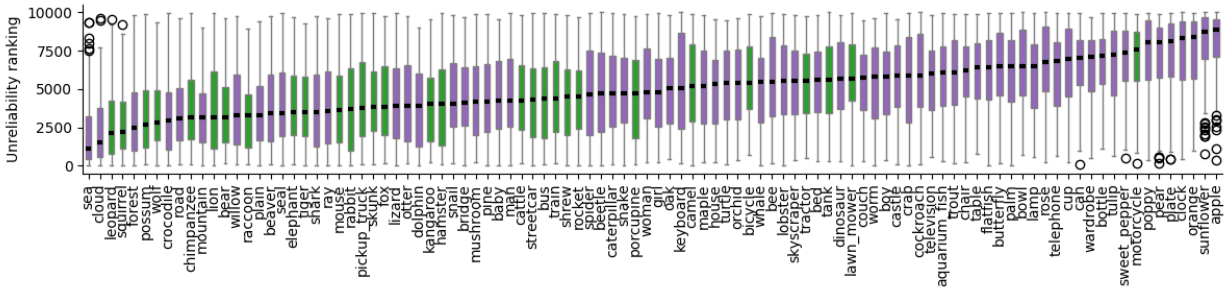

Figure 11: GP.

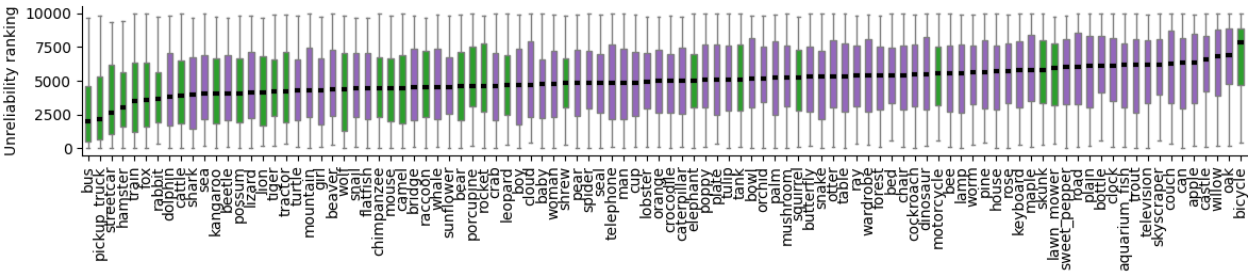

Figure 12: MC dropout.

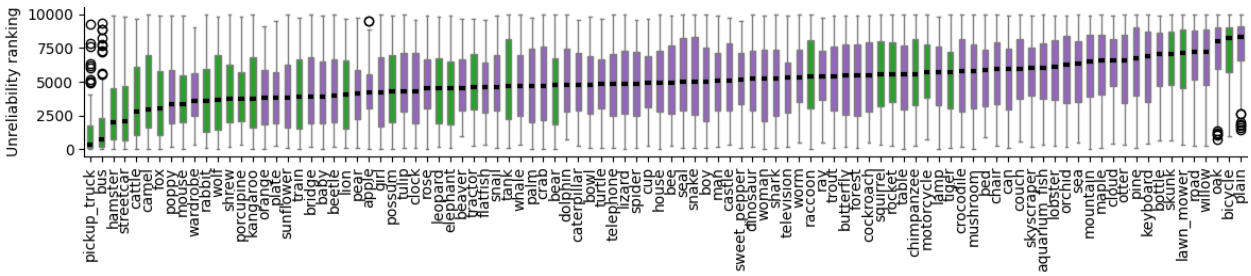

Figure 13: Cluster distance.

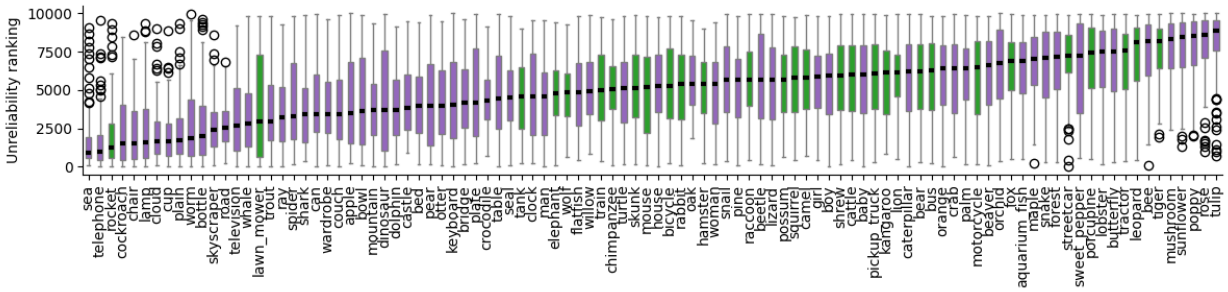

Figure 14: Residual flows density.